Received 22 October 2015; revised 6 December 2015; accepted 9 December 2015. Date of publication 12 January 2016; date of current version 23 February 2016. The review of this paper was arranged by Editor M. Chan.

Digital Object Identifier 10.1109/JEDS.2016.2517190

Physical and Numerically Stable Linvill-Lump Compact Model of the *pn*-Junction

MARCEL N. TUTT (MEMBER, IEEE), AND COLIN C. McANDREW (FELLOW, IEEE)

Freescale Semiconductor Inc., Tempe, AZ 85284, USA

CORRESPONDING AUTHOR: M. N. TUTT (e-mail: mtutt@cox.net)

ABSTRACT We present a compact model of the *pn*-junction for power device analysis using a physically based and numerically stable version of the approach proposed by Linvill in the 1950s. Problems with the original Linvill formulation have been eliminated by using quasi-Fermi potentials instead of mobile carrier densities as system unknowns and by adopting the Scharfetter–Gummel stable difference approximation. The model naturally accounts for high-level injection and reverse recovery effects and is based on physical parameters such as doping densities, recombination life-times, and geometry rather than empirical parameters such as knee current and relaxation time. The model is implemented in Verilog-A and is verified by dc, small-signal, and large-signal simulations.

INDEX TERMS Pn-junctions, junctions, semiconductor devices, compact modeling.

I. INTRODUCTION

Modeling of power semiconductor devices for integrated circuit (IC) design is challenging. Key regions of power devices are lightly doped, to enable high voltage withstand capability, and during on-state operation these regions can be flooded with mobile carriers to minimize the on-state resistance. Switching losses depend in part on diffusion and recombination of the carriers in those regions, and accurate modeling of those phenomena can be difficult. Analytical approximations using the relaxation time approximation have been proposed [1], [2], however they require extraction of parameters from experimental data and do not allow investigation of performance changes from variation in doping or device dimensions.

To provide more accurate, physically-based models of power devices we have resurrected the "Linvill lump" approach to modeling [3], [4], extending it to encompass high-level injection and to significantly improve its numerical robustness. Here we provide details of our formulation using the *pn*-junction diode as an example. Our model incorporates multi-element, physical models of quasi-neutral (QN) regions coupled through a space-charge (SC) region model, and is implemented in Verilog-A. A small number of lumps are used for QN region modeling, and an analytical model is used for the SC region, rather than numerically solving Poisson's equation. The approach naturally accounts for high-level injection, the effect of ohmic resistive drops, and modeling of non-quasi-static phenomena such as reverse recovery, without the need for empirical parameters.

The structure of the paper is as follows. Section II reviews the Linvill approach and presents enhancements that overcome limitations and numerical problems encountered in the original formulation; this is our basis for QN region modeling. Section III details the boundary conditions we use and how we analytically model a SC region, which leads to a physical model of the *pn*-junction diode. Section IV presents how we model recombination and depletion charge. Section V gives details of our Verilog-A implementation, and Section VI demonstrates the effectiveness of our model by comparison with dc, small-signal, and large signal data.

II. IMPROVED BASIC LINVILL LUMP MODEL

Consider a semiconductor region divided into discrete elements, or "lumps," as in Fig. 1 [3], [4]. The carrier densities, n and p for electrons and holes, respectively, and electrostatic potential ψ, are assumed to be uniform within a given element and equal to their values at the midpoint of the element. Fig. 2 represents the electron $\mathbf{J}_n$ and hole $\mathbf{J}_p$ current flows between adjacent elements, along with the net recombination R within each element. There are 3 unknowns associated with

2168-6734 © 2016 IEEE. Translations and content mining are permitted for academic research only.
Personal use is also permitted, but republication/redistribution requires IEEE permission.
See http://www.ieee.org/publications_standards/publications/rights/index.html for more information.

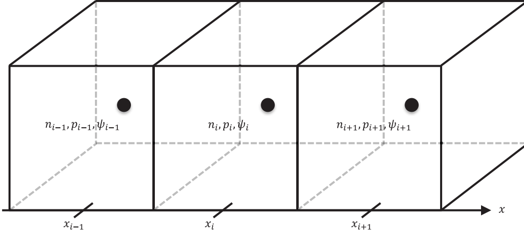

FIGURE 1. Basic Linvill-lump concept: dots are element midpoints; carrier densities and ψ are determined at the midpoint of each element.

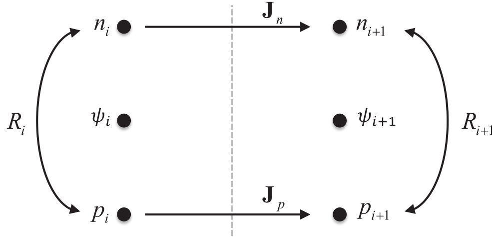

FIGURE 2. Current flows are calculated between the midpoints of adjacent elements, and recombination occurs within each element.

each element, therefore we need 3 independent equations to be able to solve for the unknowns.

The electron and hole continuity equations are:

$$\frac{1}{q}\nabla\cdot\mathbf{J}_n=\frac{\partial n}{\partial t}+R,\ \mathbf{J}_n=-q\mu_n n\nabla\phi_n \tag{1}$$

and

$$\frac{1}{q}\nabla\cdot\mathbf{J}_p=-\frac{\partial p}{\partial t}-R,\ \mathbf{J}_p=-q\mu_p p\nabla\phi_p \tag{2}$$

where q is the magnitude of the electronic charge, μ is mobility, and ϕ_n and ϕ_p are the electron and hole quasi-Fermi potentials, respectively. We assume non-degenerate doping so that the Boltzmann relations hold, i.e.,

$$p=n_{\mathrm{ie}}e^{\frac{\phi_p-\psi}{\phi_t}},\ n=n_{\mathrm{ie}}e^{\frac{\psi-\phi_n}{\phi_t}} \tag{3}$$

where n_{ie} is the effective intrinsic concentration and $\phi_t{=}kT/q$ is the thermal voltage, k being Boltzmann's constant and T the temperature in Kelvin. Integrating (1) over the lump located at x_i in Figs. 1 and 2 gives for electrons

$$\frac{J_{nx,i+\frac{1}{2}}-J_{nx,i-\frac{1}{2}}}{q}=\frac{\partial}{\partial t}\left[n\left(x_i\right)\Delta x_i\right]+R\left(x_i\right)\Delta x_i \tag{4}$$

and an analogous form for holes follows from the integral of (2) over the lump. The variables associated with each lump are ψ_i, $\phi_{n,i}$, and $\phi_{p,i}$, the values of the electrostatic and carrier quasi-Fermi potentials at x_i.

The original Linvill formulation is in terms of n and p. However, typical numerical values of these quantities span many orders of magnitude, which can introduce numerical problems when implemented in a circuit simulator that has convergence tolerances based on voltages of order a few V and currents in the range of nA to mA. Using quasi-Fermi potentials instead, as was done in [5] and is recommended in [6] for compact models, obviates that issue.

Equation (4) and the equivalent for holes are implemented as nonlinear equations, to be solved by the circuit simulator. The time dependent term and the net recombination term are the "storance" and "recombinance" elements of Linvill. In [3] and [4] the drift and diffusion components of J_{nx} are considered as separate terms, denoted driftance and diffusance, respectively. However, from the field of device simulation using these terms directly is known to be numerically unstable. We therefore compute J_{nx} using the well-known Scharfetter-Gummel stable difference approximation [7]. In its original form

$$J_{nx,i+\frac{1}{2}}=-qn_{ie}\mu_n\cdot\frac{\psi_{i+1}-\psi_i}{x_{i+1}-x_i}\cdot\frac{e^{-\phi_{n,i+1}/\phi_t}-e^{-\phi_{n,i}/\phi_t}}{e^{-\psi_{i+1}/\phi_t}-e^{-\psi_i/\phi_t}} \tag{5}$$

care must be taken during evaluation for small $\psi_{i+1}-\psi_i$. A more numerically robust form follows if $e^{(\psi_{i+1}+\psi_i)/(2\phi_t)}$ and $e^{(\phi_{n,i+1}+\phi_{n,i})/(2\phi_t)}$ are factored out giving

$$J_{nx,i+\frac{1}{2}}=-\frac{2q\phi_t\mu_n n_{ie}}{x_{i+1}-x_i}\cdot e^{(\psi_{i+1}+\psi_i-\phi_{n,i+1}-\phi_{n,i})/(2\phi_t)}\cdot\mathrm{zcsch}\left(\frac{\psi_{i+1}-\psi_i}{2\phi_t}\right)\cdot\sinh\left(\frac{\phi_{n,i+1}-\phi_{n,i}}{2\phi_t}\right) \tag{6}$$

where $\mathrm{zcsch}(z)=z\cdot\mathrm{csch}(z)$. Evaluating this function as

$$\mathrm{zcsch}(z)=\begin{cases}\dfrac{2ze^{z}}{e^{2z}-1} & \text{if } z\leq-10^{-4}\\ 1-\dfrac{z^2}{6}+\dfrac{7z^4}{360} & \text{if } -10^{-4}<z<10^{-4}\\ \dfrac{2ze^{-z}}{1-e^{-2z}} & \text{if } z\geq10^{-4}\end{cases} \tag{7}$$

is accurate to 16 digits of precision and involves only exponentials of negative arguments, so there is no possibility of numerical problems from exponential overflow. The equivalent for hole current density is

$$J_{px,i+\frac{1}{2}}=-\frac{2q\phi_t\mu_p n_{ie}}{x_{i+1}-x_i}\cdot e^{(\phi_{p,i+1}+\phi_{p,i}-\psi_{i+1}-\psi_i)/(2\phi_t)}\cdot\mathrm{zcsch}\left(\frac{\psi_{i+1}-\psi_i}{2\phi_t}\right)\cdot\sinh\left(\frac{\phi_{p,i+1}-\phi_{p,i}}{2\phi_t}\right). \tag{8}$$

One additional equation is needed to relate the quasi-Fermi potentials and the elctrostatic potential at each lump. Either the quasi-neutrality condition or Poisson's equation could be used. We have found no difference in the results when either is implemented. Enforcing quasi-neutrality is significantly simpler so that is the approach we adopted.

Space-charge neutrality in a QN p-region implies that

$$p-n-N_A=0 \tag{9}$$

where N_A is the net acceptor doping concentration, assumed uniform. While it is possible to directly substitute from (3) into (9), that leads to differences of large, similar numbers which is numerically undesirable. Rather, from (3)

$$np={n_{ie}}^2e^{(\phi_p-\phi_n)/\phi_t} \tag{10}$$

so multiplying (9) by n and introducing (10) yields, after some manipulation, the numerically stable relation

$$n = \frac{2n_{ie}e^{(\phi_p-\phi_n)/\phi_t}}{\frac{N_A}{n_{ie}} + \sqrt{\left(\frac{N_A}{n_{ie}}\right)^2 + 4e^{(\phi_p-\phi_n)/\phi_t}}}. \quad (11)$$

This constraint holds everywhere in the QN p-region, specifically it must hold at each x_i. Equating this to the second part of (3) leads to the quasi-neutrality condition for a p-doped region

$$\begin{aligned} 0 &= \psi_i - \phi_{p,i} + \phi_t \cdot \ln\left[\frac{N_A}{2n_{ie}} + \sqrt{\left(\frac{N_A}{2n_{ie}}\right)^2 + e^{(\phi_{p,i}-\phi_{n,i})/\phi_t}}\right] \\ &= \psi_i - \frac{\phi_{p,i}+\phi_{n,i}}{2} + \phi_t \cdot ln\left[\frac{N_A e^{(\phi_{n,i}-\phi_{p,i})/(2\phi_t)}}{2n_{ie}} + \sqrt{1 + \left(\frac{N_A e^{(\phi_{n,i}-\phi_{p,i})/(2\phi_t)}}{2n_{ie}}\right)^2}\right]. \end{aligned} \quad (12)$$

A similar analysis for space-charge neutrality in a uniformly n-doped QN region gives, at each x_i in that region,

$$\begin{aligned} 0 &= \psi_i - \phi_{n,i} - \phi_t \cdot \ln\left[\frac{N_D}{2n_{ie}} + \sqrt{\left(\frac{N_D}{2n_{ie}}\right)^2 + e^{(\phi_{p,i}-\phi_{n,i})/\phi_t}}\right] \\ &= \psi_i - \frac{\phi_{p,i}+\phi_{n,i}}{2} - \phi_t \cdot \ln\left[\frac{N_D e^{(\phi_{n,i}-\phi_{p,i})/(2\phi_t)}}{2n_{ie}} + \sqrt{1 + \left(\frac{N_D e^{(\phi_{n,i}-\phi_{p,i})/(2\phi_t)}}{2n_{ie}}\right)^2}\right] \end{aligned} \quad (13)$$

where N_D is the net donor doping concentration.

Note that (12) and (13) naturally embody high-level injection. Moreover, the potentials are of the order of unity, so they are numerically well scaled and they are also numerically well behaved (we use the first listed form in each equation when $\phi_{p,i}-\phi_{n,i} < 0$ and the second form when $\phi_{p,i}-\phi_{n,i} > 0$, i.e., for reverse and forward bias conditions, respectively, so evaluation of the exponentials involves only negative arguments, eliminating the possibility of exponential overflow).

In high-level injection the exponential terms in the second forms become negligible, therefore

$$\psi_i \to \frac{\phi_{p,i}+\phi_{n,i}}{2} \quad (14)$$

which also follows from (3), as $p \to n$ in high-level injection.

Kirchhoff's current law (KCL) based on (6) and (8), with (12) for p-type material or (13) for n-type material, are the 3 numerically robust equations that we formulate in Verilog-A to solve for ψ_i, $\phi_{n,i}$, and $\phi_{p,i}$ at each QN Linvill lump. Note that, in contrast to the original approach of [3], (12) and (13) are *not* defined in terms of electrical equivalents to shoe-horn into the KCL nodal analysis formulation that forms the basis of circuit simulators. Rather, they recognize that simulators are general differential algebraic equation (DAE) solvers so (12) and (13) are implemented via the technique described in [6].

III. BASIC pn-JUNCTION MODEL: BOUNDARY CONDITIONS AND THE SPACE-CHARGE REGION

To model a 1-dimensional pn-junction the device is partitioned into separate QN regions coupled by an ideal SC region, see Fig. 3. Details of carrier transport through the SC region are ignored; it is represented as a single analytical "coupling" element between two opposite polarity QN regions, so unlike TCAD models we do not spatially discretize and solve Poisson's equation and the carrier continuiy equations through the SC region. Each QN region is modeled as a series of Linvill lumps sandwiched between a contact and one boundary of the SC region element; the more QN region lumps used the more accurate the model. The length of each QN lump is taken to be the same and the lengths of the QN portions of contact and SC region lumps are one half of that value. To simplify explanation of our basic approach we will defer inclusion of recombination until the next section.

At each contact we assume space-charge neutrality and an infinite surface recombination velocity so [8]

$$\phi_p = \phi_n = V_{applied} \quad (15)$$

and for n-type material

$$\psi = V_{applied} + \phi_t \cdot ln\left[\frac{N_D}{2n_{ie}} + \sqrt{1 + \left(\frac{N_D}{2n_{ie}}\right)^2}\right] \quad (16)$$

or for p-type material

$$\psi = V_{applied} - \phi_t \cdot ln\left[\frac{N_A}{2n_{ie}} + \sqrt{1 + \left(\frac{N_A}{2n_{ie}}\right)^2}\right]. \quad (17)$$

Defining boundary conditions for the SC region is more involved; there has been some controversy in the literature as to what appropriate conditions are and recently it has been shown that in many standard text books the representations of potentials through a pn-junction are incorrect [9]. The presence of significant drift currents leads to ohmic drops in the QN regions and hence variations in potentials, so for the SC region these quantities must be considered as unknowns and not as specified by the applied terminal voltages. The classic Shockley diode analysis [10] does not account for high-level injection and assumes any change in externally applied voltage is directly reflected in carrier quasi-Fermi potential splitting across the SC region. Heasell [11] provides a summary of inconsistencies in treatments of the differences between externally applied voltage and changes in potentials across the SC region, and [12] quantifies the ohmic drop

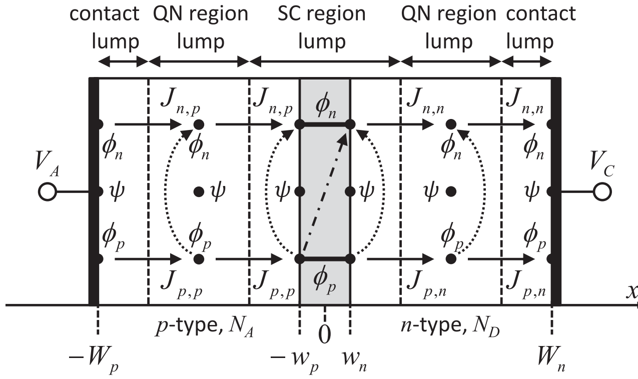

FIGURE 3. 1-dimensional *pn*-junction model. Central shaded area is the SC region; dotted arrows represent recombination current; the dot-dash arrow in the SC region is depletion capacitance current; lump indices are not shown.

for a "narrow-base" p^+-n diode under high forward bias. Unfortunately, these analyses are targeted at compact models of the complete diode, under specific assumptions such as the majority carrier current being zero, not for the general situation where (to enable NQS modeling of stored charge) there are multi-lump models of the QN regions.

Although there are really transition regions, of the order of 10 Debye lengths [13], between the edges of the "classic" depletion region and the point where the field vanishes, detailed physical simulations have shown that, serendipitously, the effect of the variation in ψ through the transition regions is essentially equivalent to, and to a large extent offsets, the effect of variation in ϕ_n and ϕ_p through the SC region [13]. This is extremely important, because it means that the SC region can be modeled as having constant quasi-Fermi potentials and being space-charge neutral at its boundaries.

For the SC region lump there appear to be 6 unknowns: the potentials at its p- and n-region boundaries, ψ_p, $\phi_{p,p}$, $\phi_{n,p}$ and ψ_n, $\phi_{p,n}$, $\phi_{n,n}$, respectively, where the added subscript indicates the doping type of the SC region boundary. The assumption, just discussed, of constant electron and hole quasi-Fermi potentials through the SC region gives

$$\phi_{p,p} = \phi_{p,n}, \ \ \phi_{n,p} = \phi_{n,n}. \tag{18}$$

Therefore, there are really only 4 unknowns; we need 4 independent equations to relate these quantities. Fig. 3 shows this by having a single value for each quasi-Fermi potential for the SC region element.

Quasi-neutrality, i.e., zero field as discussed above, at the edges of the SC region mean that eqs. (12) and (13), for the p- and n-type region edges, respectively, provide two of the equations we need to link our 4 unknowns for the SC region.

The electric field in the SC region is high, and the mobile carrier concentration there is low, so the carriers are swept through it at close to their saturated speed. This means that the recombination and charge storage terms in (4), and its equivalent for holes, are negligible. The flux of one type of carrier entering one side of the SC region must therefore (instantaneously) equal the flux of the same carrier type exiting the other side; this gives the two remaining equations needed to solve the 4 SC region unknowns. Fig. 3 depicts this, and the conditions (18), by the solid "wire" that connects the associated quasi-Fermi potential nodes across the SC region.

The edges of the SC region are not fixed but vary with the potential difference $\Delta\psi$ across the SC region. We take the metallurgical junction in Fig. 3 to be at x=0, the SC region then extends over the range $-w_p<x<w_n$ where

$$w_p = \sqrt{\frac{2\epsilon_s}{q}\frac{N_D/N_A}{N_A+N_D}}\sqrt{\Delta\psi}, \ \ w_n = \frac{N_A}{N_D}w_p. \tag{19}$$

Here ϵ_s is the permittivity of silicon. In our model the absolute length of all lumps is modified as w_p and w_n vary, the relative length is kept the same (a contact lump and each side of an SC region lump are each half the length of a QN region lump). In other words, relative spacing between the points where the potentials are calculated is kept the same, it is not just modified at the edges of the SC region as w_p and w_n vary.

Again, we stress that although we use the "ideal" depletion region width (19), which does not account for transition regions between the SC and QN regions, it was established in [13] that using that approximation in concert with the assumptions of (a) constant carrier quasi-Fermi potentials though the SC region, and (b) space-charge neutrality at the edges of the SC region, leads to serendipitous cancellation of errors from each separate assumption.

IV. RECOMBINATION CURRENT AND DEPLETION CHARGE

Recombination must be included to properly model low level currents [14] and NQS phenomena such as reverse recovery. Fortunately, it is easily included in the Linvill lump aproach. As noted previously, carrier densities in the SC region are low, so recombination there is negligible, and the contacts are assumed to be in equilibrium. Therefore, we only include recombination in QN region lumps and for the QN portions of SC region lumps.

The recombination current density in a p-type lump is

$$J_{rec} = q\Delta x\frac{n-\frac{n_{ie}^2}{N_A}}{\tau_n} \tag{20}$$

where Δx is the width of the lump, n is computed from lump system variables using (3), and τ_n is the electron lifetime. In an n-type lump

$$J_{rec} = q\Delta x\frac{p-\frac{n_{ie}^2}{N_D}}{\tau_p} \tag{21}$$

where again p is computed from lump system variables using (3) and τ_p is the hole lifetime.

The recombination current is included as the dotted arrows in Fig. 3. Note that for each side of an SC region lump Δx is half what it is for a QN region lump.

The magnitude of the depletion charge per unit area in the SC region is easily computed as

$$Q'_{\text{depl}} = w_p \cdot N_A = w_n \cdot N_D. \tag{22}$$

In an SC lump the depletion widths are already calculated from (19) so it is simple to use (22) to calculate Q'_{depl}, then $\partial Q'_{\text{depl}}/\partial t$ gives the depletion capacitance current per unit area. This flows between the SC region ϕ_p and ϕ_n nodes, see the dot-dash arrow in Fig. 3.

V. VERILOG-A IMPLEMENTATION

In the Verilog-A implementation different building-block models are defined for lumps that abut a contact, for the SC region lump, and for "normal" QN region lumps. Each lump has unknowns ψ, ϕ_n, and ϕ_p associated with it (two ψ values for an SC region lump) and these are used to code equations for all current components: transport (from (6) and (8)); recombination (from (20) and (21)); depletion charge (from (22)); and charge storage (the $\partial/\partial t$ terms from (4) and its equivalent for holes). The components of electron and hole currents are summed at the ϕ_n and ϕ_p nodes, respectively, which forces the simulator to converge to a solution that satisfies KCL for each carrier type. The charge storage and depletion charge terms are `ddt()` contributions, connected topologically as Fig. 3 shows.

Equations (12) and (13), for *p*- and *n*-type regions, respectively, are implemented internally, as described in [6], which essentially forces solution for ψ; this is done both for QN region lumps and for ψ on each side of an SC region lump. The boundary conditions defined in Section III are implemented at contact lumps, and the sum of the electron and hole current is used to form the total terminal current at each contact.

We have a generator that automatically constructs models with a specified number of lumps. The inputs to the model are the length and doping concentration of each region, and mobility and lifetime for both electrons and holes. The length of all lumps is dynamically adjusted during simulation through the variation of w_n and w_p. Because care was taken during formulation of our model all calculations are robust, numerically well behaved, and scale to values consistent with typical simulator convergence criteria, so no special tricks are required to get reliable convergence.

VI. RESULTS

To verify our model we compare it with detailed 1-dimensional TCAD simulations [15], previously reported results, and analytical expressions. The TCAD simulations were done with constant mobility, constant doping profiles and an abrupt junction, to be consistent with our Linvill lump model.

The simplest possible lump model comprises two contact lumps and one SC region lump, with no QN region

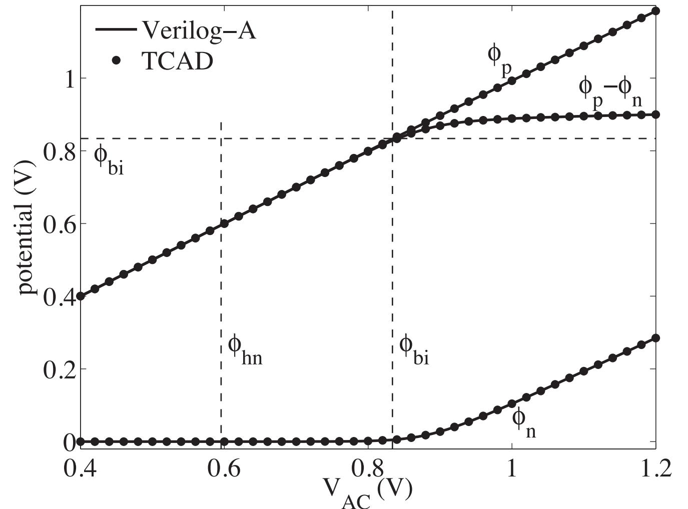

FIGURE 4. Comparison of quasi-Fermi potentials in the SC region from TCAD simulations and from a 2-lump Verilog-A model.

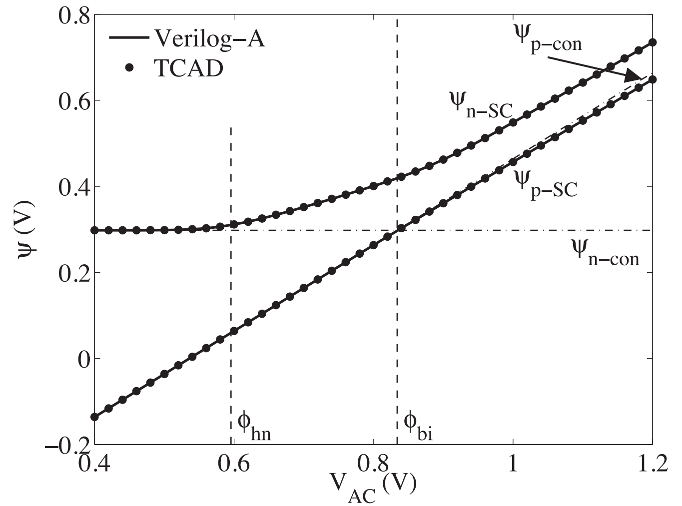

FIGURE 5. Comparison of electrostatic potentials from TCAD simulations and from a 2-lump Verilog-A model. Subscripts *p*-con and *n*-con are for the *p*- and *n*-regions contacts, respectively, and *p*-SC and *n*-SC are for the *p* and *n* sides of the SC region, respectively.

lumps. Figs. 4 through 7 compare results from this simple model with 1-dimensional TCAD simulations. For these plots $N_A = 10^{19}$ cm^{-3} and $N_D = 10^{15}$ cm^{-3}, so the built-in potential is $\phi_{\text{bi}}=(kT/q)\ln(N_A N_D/n_i^2)=0.834$ V and high-level injection on the *n*-side starts when the applied bias reaches $\phi_{\text{hn}}=2\phi_t \ln(N_D/n_i)=0.596V$, recombination is ignored for now, T=27 C, and V_C=0 V.

Fig. 4 shows quasi-Fermi potentials in the SC region, as well as the difference between them[1]; the results are essentially identical. ϕ_p increases linearly with applied bias since the *p*-side is significantly more heavily doped than the *n*-side and does not go into high-level injection, hence from (2) we have $\nabla\phi_p\approx 0$ through the *p*-region. ϕ_n stays approximately at

1. The quasi-Fermi potentials at the contacts are set equal to the applied potentials, see (15), so for clarity are not shown.

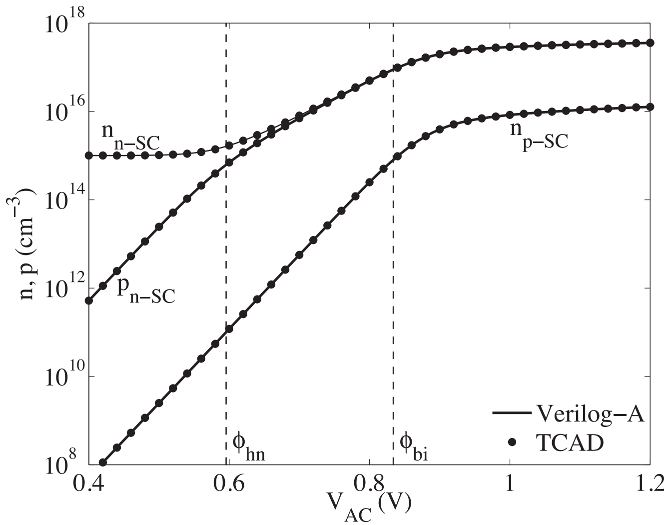

FIGURE 6. Comparison of carrier densities from TCAD simulations (symbols) and from a 2-lump Verilog-A model (solid lines). Subscripts *p*-SC and *n*-SC are for the *p* and *n* sides of the SC region, respectively.

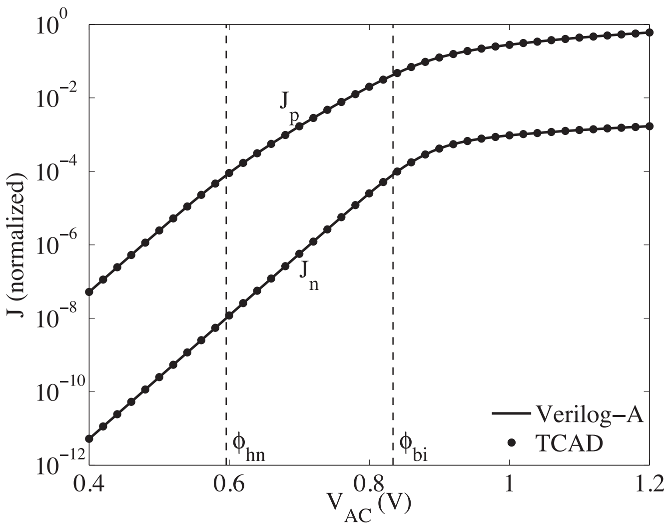

FIGURE 7. Comparison of current densities through the SC region from TCAD simulations (symbols) and from a 2-lump Verilog-A model (solid lines).

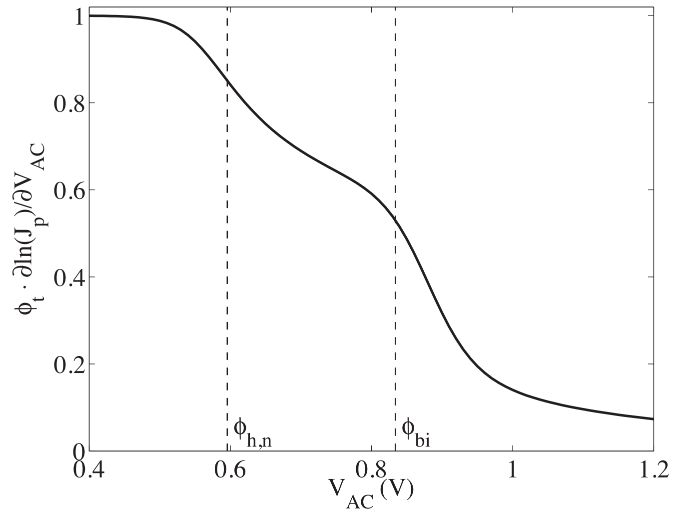

FIGURE 8. $(\phi_t/J_p)\cdot\partial J_p/\partial V_{AC}$ for the data of Fig. 7.

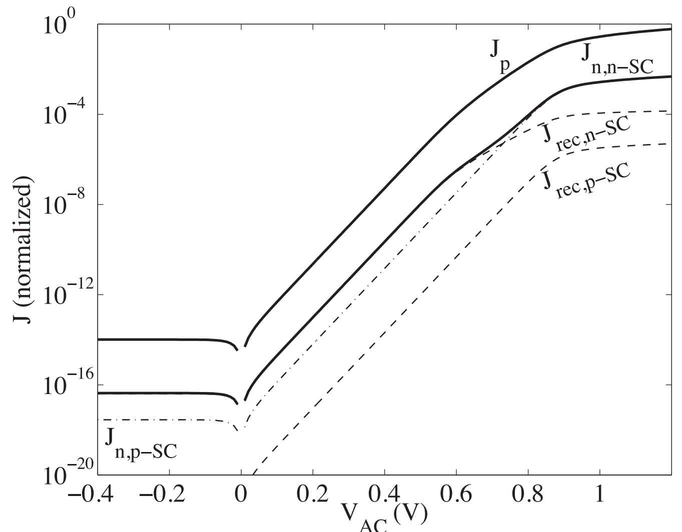

FIGURE 9. Effect of recombination. J_{rec} is the recombination current density, which is the same for electrons and holes, and *p*-SC and *n*-SC indicate the *p* and *n* sides of the SC region, respectively.

the potential applied to the cathode, 0 V, until $\phi_p - \phi_n$ through the SC region approaches ϕ_{bi}. For higher applied bias the ohmic drop across the *n*-region causes ϕ_n to increase.

Fig. 5 shows the electrostatic potentials at both the contacts and the edges of the SC region. From (16) and (17) ψ at the *n*-contact is constant and at the *p*-contact increases linearly with the applied bias V_{AC}, and since there is little ohmic drop across the *p* region because of its high doping ψ at the *p*-side SC region edge essentially tracks its value at the contact. In the *n*-region ψ at the SC region edge increases once the *n*-side goes into high-level injection, from (3) to pull n above N_D because, per Fig. 4, ϕ_n is still near zero. The slope $\partial\psi/\partial V_{AC}$ increases further when the ohmic drop across the *n*-region becomes observable and ϕ_n increases as V_{AC} increases.

Fig. 6 shows the mobile carrier densities at the edges of the SC region. p on the *n*-side varies from low-level injection to well into high-level injection. Moreover, n clearly adjusts to maintain quasi-neutrality. The *p*-side remains in low-level injection.

Fig. 7 shows (normalized) hole and electron current densities through the SC region. Three regions are apparent: low-level injection for $V_{AC} < \phi_{hn}$; high-level injection for $\phi_{hn} \lessapprox V_{AC} \lessapprox \phi_{bi}$; and where the ohmic drop in the lightly doped *n*-region is significant for $V_{AC} > \phi_{bi}$. These regions are more distinct if the derivative of the current density is plotted, see Fig. 8.

Despite the simplicity of the model with two contact lumps, one SC region lump, and no QN region lumps,

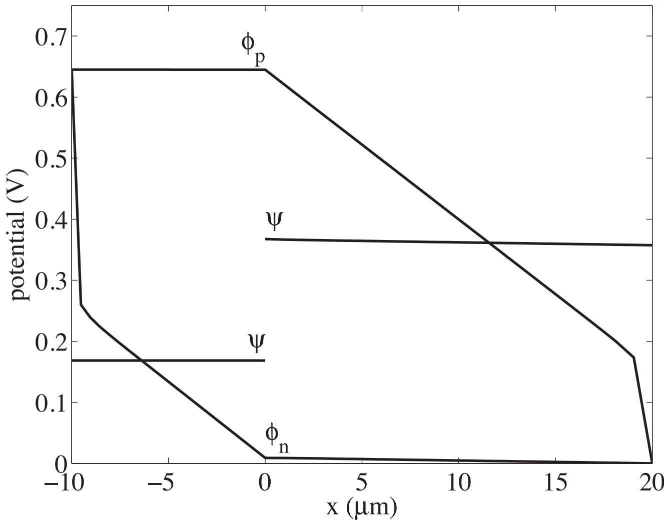

FIGURE 10. Potential distributions through a diode at low current density; position is with respect to SC region edges.

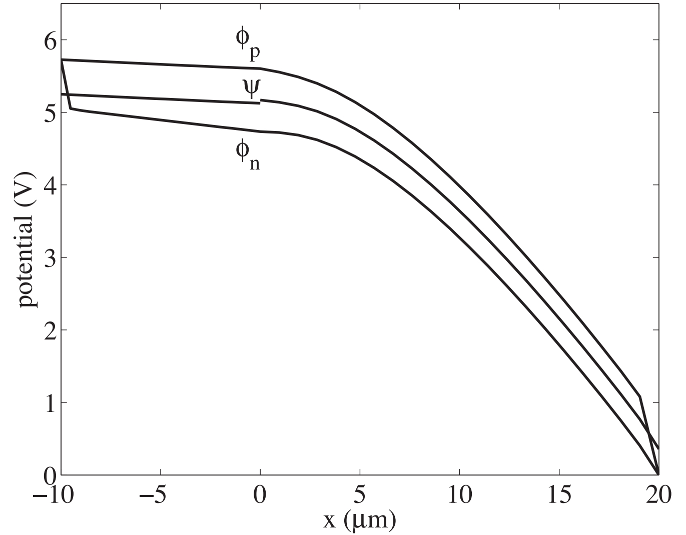

FIGURE 12. Potential distributions through a diode at high current density; position is with respect to SC region edges.

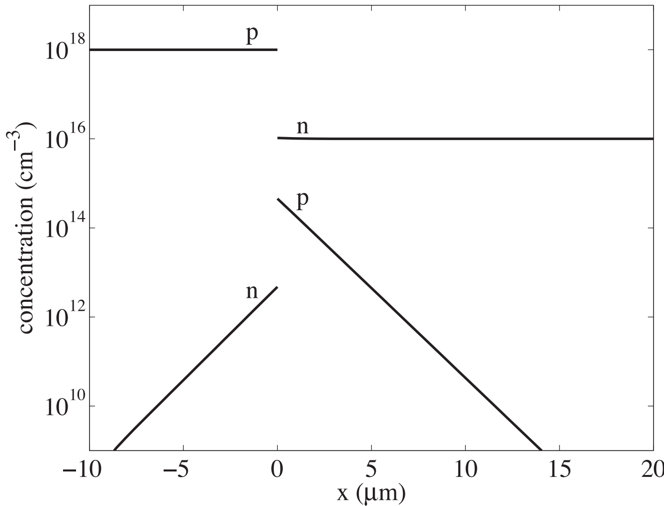

FIGURE 11. Carrier concentrations through a diode at low current density; position is with respect to SC region edges.

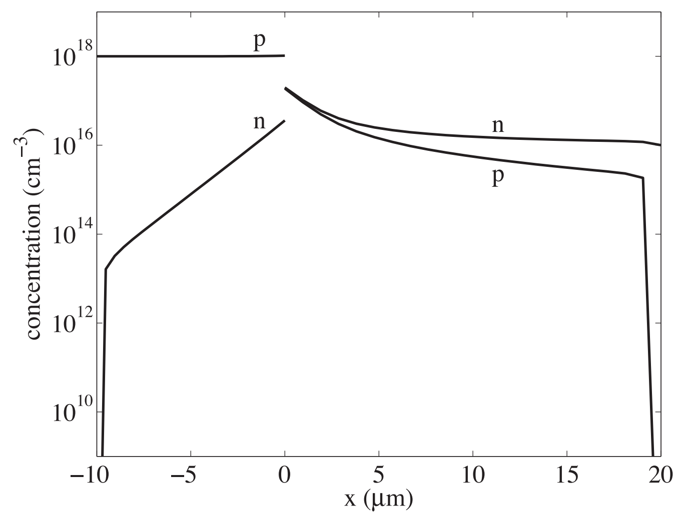

FIGURE 13. Carrier concentrations through a diode at high current density; position is with respect to SC region edges.

Figs. 4 through 7 show that it agrees quite well with much more detailed TCAD simulations.

Adding recombination, with $\tau_n=\tau_p=0.1$ μs, gives the results of Fig. 9. From (20) and (21) the majority of the recombination will be on the *n* side, and will increase the electron current density, compare Figs. 7 and 9. The slight decrease in J_p is not visible in these plots. In Fig. 9 we include negative and low forward bias across to *pn*-junction, to verify that our model works reliably for these biases.

Detailed analysis of potentials and carrier concentrations through a p^+n-junction under both low- and high-level injection conditions were provided in [16]. To further verify the accuracy of our approach we generated a model with 20 QN region lumps per side using the same material parameters as [16]: $N_A=10^{18}$ cm^{-3}, $N_D=10^{16}$ cm^{-3}, $W_p=10$ μm, $W_n=20$ μm, $\mu_p=490$ cm^2/(V·s), $\mu_n=1360$ cm^2/(V·s), $\tau_n=0.3$ ns, and $\tau_p=0.84$ ns. Figs. 10 and 11 show the potentials and carrier concentrations through the diode in low-level injection, with a current density of 10 A/cm^2 ($V_{AC}=0.645$ V), and Figs. 12 and 13 show the same quantities under high-level injection, with a current density of 10^4 A/cm^2 ($V_{AC}=5.725$ V). The results match those of [16], and show the expected behavior. In particular, under high-level injection the increase in the mobile electron concentration on the *n*-side, to maintain quasi-neutrality as the injected hole concentration exceeds N_D, is apparent, as is the significance of the ohmic drop through the lightly doped *n* region. Our model is intended for circuit simulation, not TCAD type simulation, but because of its physical nature is capable of the latter (but with an analytical, not numerical, model for the SC region).

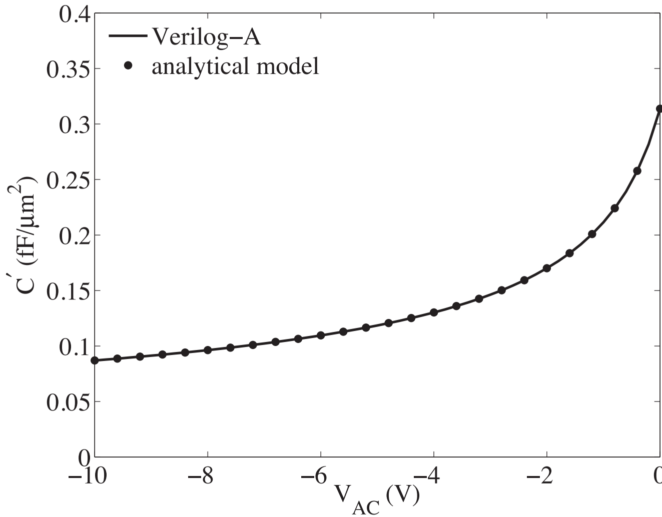

FIGURE 14. Depletion capacitance in reverse bias, N_A=10^{18} cm^{-3} and N_D=10^{16} cm^{-3}.

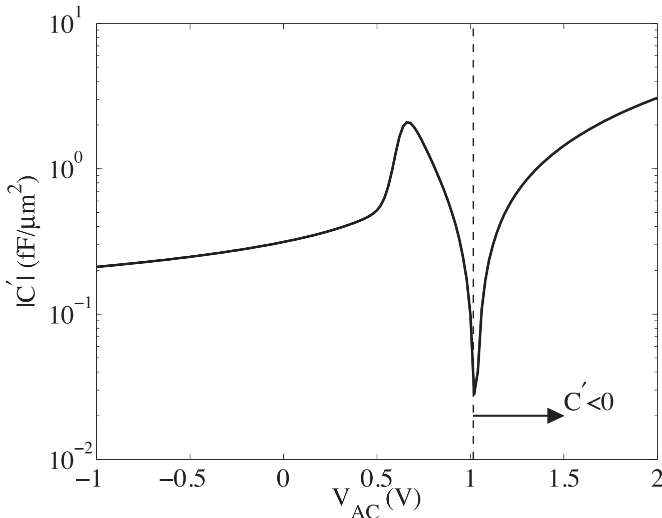

FIGURE 15. Capacitance in forward bias, N_A=10^{18} cm^{-3} and N_D=10^{16} cm^{-3}; the capacitance is negative for V_{AC}>1.02 V.

In reverse bias the capacitance per unit area of an abrupt *pn*-junction should be

$$C'_{\text{depl}}(V_{AC}) = \frac{C'_{\text{j0}}}{\left(1 - \frac{V_{AC}}{\phi_{\text{bi}}}\right)^m} \tag{23}$$

where m is the grading coefficient, 0.5 for an abrupt junction, and $C'_{\text{j0}}=\sqrt{q\epsilon_s N_A N_D/[2\phi_{\text{bi}}(N_A+N_D)]}$ is the zero-bias capacitance per unit area. Fig. 14 compares results from our model (using 5 QN region lumps per side) with the analytical model (23); the results are essentially identical, as expected because our SC region model is based on the same assumptions that underly (23). The reactance of a strongly forward biased *pn*-junction can become more complicated, as discussed by Laux and Hess [13]. For a narrow-base diode, the

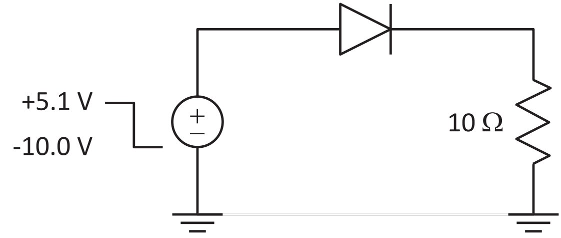

FIGURE 16. Reverse recovery simulation circuit.

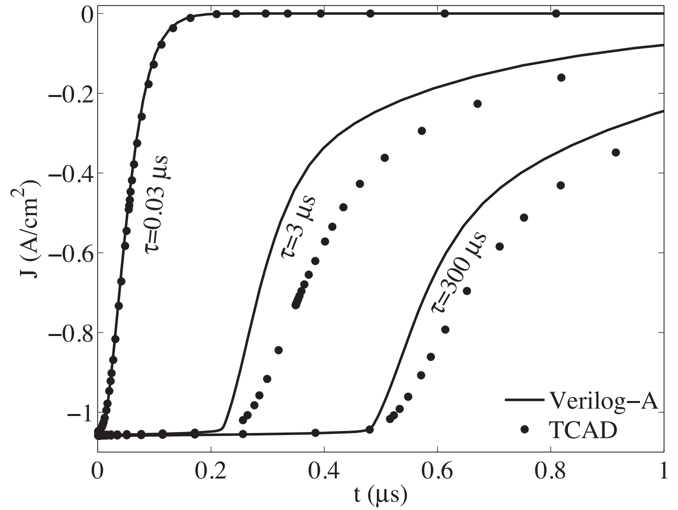

FIGURE 17. Reverse recovery behavior for different lifetimes, τ_p=τ_n=τ.

reactance not only drops, but it can become negative, displaying an inductive behavior. Fig. 15 shows that our model correctly exhibits this behavior.

Our final model verification test is for the transient response of a diode that is switched from the on-state to the off-state; this is the well-known reverse recovery behavior. We use a diode with an area of 1.0 cm^2, four QN lumps for each side, and: N_A=10^{19} cm^{-3}, N_D=10^{15} cm^{-3}, W_p=10 μm, W_n=100 μm, μ_p=490 cm^2/(V·s), μ_n=1360 cm^2/(V·s), τ_n=τ_p=0.03, 3.0, and 300.0 μs. Fig. 16 shows the circuit schematic. Initially, the diode and series resistor are forward biased with +5.1V. At t=0 the voltage source is switched to −10 V. At this point, the current through the diode reverses direction. During the storage period the current remains constant. After the storage time has been reached, the diode enters the recovery phase, during which the current current decays to zero. As Fig. 17 shows, our Linvill lump based model exhibits the same qualitative behavior as detailed TCAD simulation (fine details of the simulation are not reproduced exactly because the TCAD simulations use significantly more sophisticated recombination, and other, models than (20) and (21), and have a significantly finer spatial discretization).

VII. CONCLUSION

We have successfully applied and extended the Linvill approach to physically model *pn*-junctions. Numerical

problems with the original Linvill formulation were eliminated by adopting quasi-Fermi potentials instead of mobile carrier densities as system unknowns and by using the Scharfetter-Gummel stable difference approximation. We also used charge neutrality, rather than solving Poisson's equation, to determine ψ and significantly improved modeling of the space-charge region. The model was implemented in Verilog-A and verified by comparison with dc, small-signal, and large-signal results from detailed numerical simulations. Although the approach involves mapping the basic semiconductor equations into a difference form for QN region lumps, akin to a TCAD model, rather than an analytical solution, it converges robustly and runs fast enough for use in circuit simulation. We are using the approach as the basis for physical modeling of IGBTs and power bipolar transistors for circuit design, and plan to investigate its applicability for *pin*-diodes.

The main assumptions that affect the accuracy of our model are: abrupt junctions; a simplified model of the SC region; ideal contacts; constant mobility; constant lifetimes; constant doping density in each QN region; and negligible impact ionization. The first two of these are inherent in our model formulation. The next three can be implemented fairly simply, with only a small impact on model complexity. The final two are not as simple to include without significantly increasing model simulation time, and we are looking into efficient ways to incorporate them, without compromising computational efficiency.

ACKNOWLEDGMENT

The authors would like to thank Dr. Olin Hartin for the TCAD simulations used to confirm the reverse recovery simulations of our model.

REFERENCES

[1] P. O. Lauritzen and C. L. Ma, "A simple diode model with reverse recovery," *IEEE Trans. Power Electron.*, vol. 6, no. 2, pp. 188–191, Apr. 1991.
[2] A. T. Yang, Y. Liu, and J. T. Yao, "An efficient nonquasi-static diode model for circuit simulation," *IEEE Trans. Comput.-Aided Design Integr. Circuits Syst.*, vol. 13, no. 2, pp. 231–239, Feb. 1994.
[3] J. G. Linvill, "Lumped models of transistors and diodes," *Proc. IRE*, vol. 46, no. 6, pp. 1141–1152, Jun. 1958.
[4] J. G. Linvill and J. F. Gibbons, *Transistors and Active Circuits*. New York, NY, USA: McGraw Hill, 1961.
[5] T. Ohtsuki and K. Kani, "A unified modeling scheme for semiconductor devices with applications of state-variable analysis," *IEEE Trans. Circuit Theory*, vol. CT-17, no. 1, pp. 26–32, Feb. 1970.
[6] C. C. McAndrew *et al.*, "Best practices for compact modeling in Verilog-A," *IEEE J. Electron Devices Soc.*, vol. 3, no. 5, pp. 383–396, Aug. 2015.
[7] D. L. Scharfetter and H. K. Gummel, "Large-signal analysis of a silicon read diode oscillator," *IEEE Trans. Electron Devices*, vol. ED-16, no. 1, pp. 64–77, Jan. 1969.
[8] W. L. Engl, H. K. Dirks, and B. Meinerzhagen, "Device modeling," *Proc. IEEE*, vol. 71, no. 1, pp. 10–33, Jan. 1983.
[9] X. Yang and D. K. Schroder, "Some semiconductor device physics considerations and clarifications," *IEEE Trans. Electron Devices*, vol. 59, no. 7, pp. 1993–1996, Jul. 2012.
[10] W. Shockley, "The theory of $p-n$ junctions in semiconductors and $p-n$ junction transistors," *Bell Syst. Tech. J.*, vol. 28, no. 3, pp. 435–489, Jul. 1949.
[11] E. L. Heasell, "Boundary conditions at p-n junctions," *Solid-State Electron.*, vol. 22, no. 10, pp. 853–856, Oct. 1979.
[12] D. J. Roulston, *Bipolar Semiconductor Devices*. New York, NY, USA: McGraw-Hill, 1990.
[13] S. E. Laux and K. Hess, "Revisiting the analytic theory of $p-n$ junction impedance: Improvements guided by computer simulation leading to a new equivalent circuit," *IEEE Trans. Electron Devices*, vol. 46, no. 2, pp. 396–412, Feb. 1999.
[14] C.-T. Sah, R. N. Noyce, and W. Shockley, "Carrier generation and recombination in $p-n$ junctions and $p-n$ junction characteristics," *Proc. IRE*, vol. 45, no. 9, pp. 1228–1243, Sep. 1957.
[15] *Sentaurus Device User Guide Version G-2012.06*, Synopsys, Mountain View, CA, USA, 2012.
[16] H. K. Gummel, "Hole-electron product of *pn* junctions," *Solid-State Electron.*, vol. 10, no. 3, pp. 209–212, Mar. 1967.

MARCEL N. TUTT (M'96) received the Ph.D. degree from the University of Michigan, Ann Arbor, MI, USA, in 1992, and the B.A.Sc. and M.A.Sc. degrees from the University of Waterloo, Waterloo, ON, Canada, in 1980 and 1983, respectively, all in electrical engineering. He has worked in the areas of microwaves and millimeterwaves (mmW) for over 20 years. At Texas Instruments, he worked on III-V HBT circuit designs for low AM noise and radar applications. He joined Freescale, where he developed the modeling process for their III-V HBTs for handset PA applications. Later, he managed Freescale's III-V device modeling and characterization group and supervised the development of on-wafer mmW test systems for the characterization of mmW devices and circuits. He has published in the areas of modeling and measurement techniques and recently, he has become involved in the modeling and characterization of high power switching devices (MOSFETs and IGBTs) for automotive applications.

COLIN C. McANDREW (S'82–M'84–SM'90–F'04) received the B.E. (Hons.) degree in electrical engineering from Monash University, Melbourne, Australia, in 1978, and the M.A.Sc. and Ph.D. degrees in systems design engineering from the University of Waterloo, Canada, in 1982 and 1984, respectively. From 1987 to 1995, he was with AT&T Bell Laboratories, Allentown, PA, USA. Since 1995, he has been with Freescale Semiconductor (formerly Motorola Semiconductor Products Sector), Tempe, AZ, USA, where he is currently a Freescale Fellow. He was a recipient of the Best Paper Award from ICMTS in 1993 and 2012 and CICC in 2002, the BCTM Award in 2005, and the SRC Mahboob Khan Outstanding Mentor Award in 2007. He was an Editor of the IEEE TRANSACTIONS ON ELECTRON DEVICES from 2001 to 2010. He has been an Editor of the IEEE JOURNAL OF THE ELECTRON DEVICES SOCIETY since 2013. He is or has been on the Technical Program Committee for the IEEE BCTM, ICMTS, CICC, and BMAS conferences.